Fabrication and characterization of hardystonite-chitosan biocomposite scaffolds

Silvia Stella Ramirez Caballero, Hamada Elsayed, Solene Tadier, Alexandra Montembault, Eric Maire, Laurent David, Thierry Delair, Paolo Colombo, Laurent Gremillard

Fabrication and characterization of hardystonite-chitosan biocomposite scaffolds

Published in Journal of Ceramics International (2019) 45[7] p. 8804-8814
https://doi.org/10.1016/j.ceramint.2019.01.206

Silvia Stella Ramirez Caballero[a,b], Hamada Elsayed[c,d], Solène Tadier[a], Alexandra Montembault[b,*], Eric Maire[a], Laurent David[b], Thierry Delair[b], Paolo Colombo[c,e], Laurent Grémillard[a,*]

[a] *Univ Lyon, INSA Lyon, Université Claude Bernard Lyon 1, CNRS, MATEIS UMR5510, F-69621 Villeurbanne, France*
[b] *Univ Lyon, Université Claude Bernard Lyon 1, CNRS, Ingénierie des Matériaux Polymères, IMP@Lyon1, UMR 5223, F-69622 Villeurbanne, France*
[c] *Dipartimento di Ingegneria Industriale, University of Padova, Via Marzolo 9, 35131 Padova, Italy*
[d] *Ceramics Department, National Research Centre, El-Bohous Street, 12622 Cairo, Egypt*
[e] *Department of Materials Science and Engineering, the Pennsylvania State University, University Park, PA 16801, USA*

[*] *Corresponding authors:*
Alexandra Montembault: alexandra.clayer-montembault@univ-lyon1.fr ; +33 (0)4 78 77 87 35
Laurent Gremillard: laurent.gremillard@insa-lyon.fr; +33 (0)4 72 43 81 52

Abstract

Hardystonite scaffolds produced by ceramization of 3-D printed preceramic filled polymer were impregnated with chitosan solutions, later neutralized into physical hydrogels. Hardystonite bioceramic and chitosan physical hydrogel were chosen for their interesting biological properties as potential bone substitutes. Five impregnation protocols, differing in impregnation vacuum, chitosan concentration, chitosan to hardystonite mass ratio and base used for chitosan gelation were studied. The composition, micropore structure and surface morphology of impregnated scaffolds were determined. Impregnated hardystonite scaffolds were tested to find out the effect of impregnation protocols on elastic and dissipative mechanical properties of the composites. The capacity for energy dissipation and for load bearing increased as chitosan content increased in the composites. Thus, 3-D architectured biocomposites with enhanced mechanical properties can be manufactured following the method shown in this article.

Keywords: direct ink writing, physical hydrogels, polymer impregnation, bone substitutes, ceramic-polymer composites, fracture.

1. Introduction

The high prevalence of bone diseases and fractures is a major societal problem, especially for elderly people. For example, it is estimated that 10.2% of the population suffered from osteoporosis in the United States in 2010 [1] (with projections to 12.3% in 2020 and 13.6% in 2030), with increased risk of bone fractures compared to population with healthy bones. With the increase in life expectancy, designing efficient solutions for bone repair has become a major research area in the last decades. Among these solutions, bone tissue engineering aims at combining biomaterials, cells and growth factors to obtain bone graft substitutes with optimized properties [2].

Several materials in different physical forms have been used for bone tissue engineering. Materials include bioactive glasses, bioceramics, biopolymer composites reinforced by inorganic fillers, as well as polymer-coated or infiltrated ceramics and organic–inorganic composites. 3-D scaffolds, pellets, cements pastes [3], fibrous materials [4] are example of possible physical forms.
Among composite scaffolds, impregnation of ceramics with polymers has been widely reported in the literature [2,3,5–10]. Ceramic scaffolds have mostly been impregnated with synthetic polymers such as polycaprolactone (PCL), poly-DL-lactide (PDLLA) or poly(lactic-co-glycolic acid) (PLGA). More recently, polymers of natural origin, such as gelatin, silk, alginate, collagen and chitosan, have also been used [3].
The addition of a soft biodegradable polymer to inorganic scaffolds may provide two advantages. First, under certain conditions the toughness or strength of the composite may be higher than those of the inorganic scaffold alone. Second, the biodegradable polymer can be used as a vehicle for controlled *in-situ* delivery of bioactive molecules, for example, growth factors [3] or adhesion peptides [11,12].

Hardystonite ($Ca_2ZnSi_2O_7$, HT) is a ceramic of interest for biomedical use thanks to its biological properties. It has been shown to increase proliferation and osteogenic differentiation of mesenchymal stem cells [13,14]. Furthermore, it stimulates the expression of alkaline phosphatase, osteocalcin and type I collagen when in contact with human osteoblast-like cells [14,15]. The mechanical properties of hardystonite are also interesting. The bending strength of dense HT is in the 50-140 MPa range, reaching the values of human cortical bone (50-150 MPa). Its Young's modulus lies between 20 and 40 GPa, also close to that of cortical bone (7-30 GPa) [16,17]. However, in order to increase cell colonization and cytocompatibility, a relatively high porosity is needed [18], limiting the strength of the material. Hardystonite has shown better biocompatibility, bending strength and fracture toughness than hydroxyapatite ($Ca_{10}(PO_4)_6(OH)_2$) [14,16,19,20].
Chitosan is a copolymer of N-acetyl-glucosamine and glucosamine units, obtained by deacetylation of chitin. Chitin is one of the most abundant polysaccharides on earth, found in particular in the exoskeleton of crustaceans and insects, and in the endoskeleton of cephalopods [21,22]. Thus, chitin extraction can be considered as valorization of waste from the fish industry. Chitosan is a non-toxic and biodegradable natural polymer [23,24]. It is known to promote osteoblast and mesenchymal cell formation and *in-vivo* vascularization [25–27]. In particular, chitosan-based hydrogels have promising properties for bone substitution, such as angiogenicity, biodegradability, antimicrobial activity and low toxicity [24,28-31].
The physical gelation of a chitosan solution can occur at neutral or alkaline pH, and it is due to a modification of the balance between hydrophilic and hydrophobic interactions within the solution [32]. Gelation occurs when an aqueous solution of chitosan is in contact with a base, e.g., ammonia [32] or sodium hydroxide [33]. No external crosslinking agent is necessary for this gelation process. Chitosan dissolves in acid aqueous medium, due to the presence of protonated amine groups that promote hydrophilic interactions [33,23]. The neutralization of the protonated amine groups of chitosan in solution results in the gelation of the solution, if the polymer concentration is above a critical value [32].

As a summary, a composite of HT and CS could possess the adequate combination of properties for a bone substitution material: angiogenicity, osseoconductivity and sufficient mechanical properties. Surprisingly, although a few studies on inorganic scaffold impregnation by chitosan have been reported in the literature [34–37], no article studying the association of hardystonite scaffolds with chitosan physical hydrogels was found. Thus the present article deals with the preparation and characterization of hardystonite (HT) and chitosan (CS) composite materials. The aims are to develop protocols for fabricating HT scaffolds impregnated with CS physical hydrogel and to find out the effect of impregnation on the mechanical properties of the composites.
HT scaffolds of specific geometry were produced by additive manufacturing (Direct Ink Writing, DIW) with an ink based on a preceramic polymer containing reactive powder fillers and additives, followed by ceramization by heat treatment in air at high temperature [14]. HT scaffolds were then impregnated with chitosan solutions, which were then neutralized to obtain hardystonite- chitosan physical hydrogel composites (HT-CS).
Crystalline phase identification and porosity measurements of HT and HT-CS materials were carried out. The fracture surfaces of HT-CS scaffolds were analyzed to investigate the repartition of chitosan in the pores and polymer-ceramic interfaces. Fracture behavior (in particular compressive strength and mechanical energy dissipation) was assessed for HT and HT-CS scaffolds.

2. Materials and Methods

2.1. Fabrication of 3-D hardystonite scaffolds

The manufacturing of 3-D Hardystonite scaffolds (HT scaffolds) was carried out in three steps: i) design and formulation of the printing ink, ii) printing of a preceramic-filled system of specific geometry and iii) formation of hardystonite ceramics (ceramization).
The preceramic ink was designed and prepared with the aim of obtaining pure hardystonite after heat treatment. A commercially available silicone resin, MK (Silres MK polymethylsilsesquioxane, in the form of powder <100 µm, Wacker Chemie, Germany) was dissolved in isopropanol alcohol under stirring. To modify the ink rheology and provide a suitable pseudo-plastic behavior, silicone resin and fumed silica (FS, Aerosil R106, Evonik, Essen, Germany) were mixed in a weight ratio of 90MK:10FS. Powders of calcium carbonate, $CaCO_3$ (< 10 µm; Bitossi, Italy) and zinc oxide, ZnO (d_{50} = 14 µm; Sigma Aldrich, Germany) were added as active fillers in the appropriate molar ratio to obtain a pure hardystonite phase ceramic as a final product after ceramization. 30 wt% hardystonite powder, previously synthesized under the same procedure and ground to <45µm, was added to the mixture to improve its final quality (see below). The materials required to prepare the preceramic ink were mixed in an agate jar with agate balls (diameter ~1 cm) using a planetary ball mill for 4h at 400 rpm.
A printer equipped with a syringe (Powerwasp Evo, Wasp, Massa Lombarda, Italy) was used to fabricate HT scaffolds [38], with dimensions 15 × 5 × 5 mm^3, 1 mm spanning length between the center of two contiguous filaments in the same layer, and layer thickness of 0.35 mm. The ink was placed into a syringe and extruded at room temperature through a conical nozzle (0.41 mm internal diameter, Nordson Italia S.p.A., Milano, Italy).
High purity hardystonite ceramics were obtained by heating in air the preceramic-filled system according to a multi-step thermal treatment (preheating at 200°C on a PTFE foil to initiate the cross linking of the polymer, then 1°C/min up to 450°C, 0.5°C/min up to 500°C (1h dwell), 0.5°C/min up to 600°C (3h dwell), 1°C/min to 900°C, 5°C/min to 1200°C (1h dwell) then cooling down to room temperature at ~5°C/min) [38]. This thermal treatment was designed to minimize the crack formation caused by carbon dioxide released from the decomposition of calcium carbonate. The crack formation was also minimized by the addition of 30 wt.% hardystonite powder in the ink, as mentioned above.

2.2. Preparation of hardystonite-chitosan physical hydrogel composite

Preparation of hardystonite-chitosan composites (HT-CS) involved three steps: preparation of the chitosan solution, impregnation of 3D hardystonite scaffolds with chitosan solution and finally, gelation to form *in situ* the chitosan physical hydrogel.

Chitosan powder produced from squid pens, and supplied by Mahtani Chitosan Pvt. Ltd (batch type 114, No S3 20110121), was used. It was characterized before use, as previously described [32]. The degree of acetylation, corresponding to the molar fraction of acetylated units, was close to 5%; the weight-average molar mass and the dispersity were M_w=550 kg.mol^{-1} and Đ=1.9, respectively.

Three chitosan solutions were prepared (at 0.03, 0.09 and 0.15M of repeat units i.e. 0.5, 1.5 and 2.5 wt% respectively) by adding chitosan powder to an acetic acid aqueous solution (acetic acid: Carlo Erba Reagents, CAS 64-19-7, assay 99.9%). The amount of acetic acid was adjusted to match the stoichiometric protonation of -NH_2 sites of chitosan. The complete dissolution of chitosan was obtained after several mixing cycles of five minutes at 3000 rpm, using a speed mixer (DAC150.1FVZ-K, Synergy devices Ltd, UK).

Impregnation of HT scaffolds with chitosan solutions was carried out following five different protocols (varying degree of impregnation vacuum, concentration of chitosan, and base used for gelation), see Table 1. In all cases, a HT scaffold of known weight and a chitosan solution of known volume were kept separately in a single desiccator and outgassed for 1h under controlled pressure (later referred to as "impregnation vacuum"), using a vacuum pump. While still under vacuum, the HT scaffold was dropped into the chitosan solution and left to rest for 25 min. After vacuum release, the resulting sample was dropped into a second chitosan solution of known volume (2.5 mL), at atmospheric pressure. The impregnated system was then kept for 85 minutes under the same vacuum as in the first impregnation (see Table 1). Since the pressure during impregnation (50 or 80 mbar) was kept significantly higher than the saturation vapor pressure (32 mbar at 25°C), water evaporation during impregnation was considered negligible. As a result, the chitosan concentration was considered as constant during the whole impregnation process. Then, chitosan gelation was performed either by immersion for 1h in a 25 mL of a 1M NaOH solution (NaOH: Carlo Erba Reagents, CAS 1310-73-2, assay ≥ 97%), or by exposure for 22h to an ammonia atmosphere provided by 25 mL of a 1M NH_4OH solution (Sigma-Aldrich, CAS 1336-21-6, assay 28-30%). After gelation, the HT-CS scaffolds were washed several times, until a stable pH value of ~ 7 was measured in the washing water. The HT-CS scaffolds were weighed at each step of the process. They were kept in distilled water until further characterizations. Samples were labeled HT-CS-x, with x being the protocol number used, as referred to in Table 1.

To investigate the effect of chitosan hydrogel on the mechanical properties of HT-CS scaffolds, the chitosan weight content and concentration were calculated at each step of their fabrication. Each sample was weighed before impregnation (m_0), after the first impregnation (m_1), after the second impregnation (m_2), and after gelation and washing (m_g).

Weights gained after each impregnation with chitosan solution and after gelation (before washing) were calculated using the following straightforward relations:

$$weight\ gained\ after\ 1st\ imp.(g) = {m_{sol}}^{1-0} = m_1 - m_0 \quad (1)$$

$$weight\ gained\ after\ 2nd\ imp.(g) = {m_{sol}}^{2-1} = m_2 - m_1 \quad (2)$$

$$weight\ gained\ after\ gelation\ and\ washing\ (g) = {m_{sol}}^{g-2} = m_g - m_2 \quad (3)$$

The weight of chitosan (CS) gained after each impregnation was calculated:

$$CS\ gained\ during\ 1st\ imp.\ (g)\ =\ {m_{CS}}^{1-0} = {m_{sol}}^{1-0} * [CS_{1st}] \quad (4)$$

$$CS\ gained\ during\ 2nd\ imp.\ (g)\ =\ {m_{CS}}^{2-1} = {m_{sol}}^{2-1} * [CS_{2nd}] \quad (5)$$

The resulting chitosan concentration after the second impregnation was then calculated:

$$CS\ resulting\ after\ 2nd\ imp.\ (wt\%) =\ [CS_r] = \frac{{m_{CS}}^{1-0} + {m_{CS}}^{2-1}}{{m_{sol}}^{1-0} + {m_{sol}}^{2-1}} \quad (6)$$

Gelation was carried out for the HT-CS scaffolds at the chitosan concentration obtained after the second impregnation, $[CS_r]$. Therefore, the weight of chitosan gained during gelation (${m_{CS}}^{g-2}$) could be calculated using eq. 7:

$${m_{CS}}^{g-2} = {m_{sol}}^{g-2} * [CS_r] \quad (7)$$

Knowing the weight of chitosan in the sample and the weight of HT scaffold, a CS/HT ratio was finally calculated as:

$$\frac{CS}{HT} = \frac{{m_{CS}}^{1-0} + {m_{CS}}^{2-1} + {m_{CS}}^{g-2}}{m_{HT}} \quad (8)$$

2.3. Microstructural characterizations

Dimensions of HT scaffolds were measured after ceramization by means of a digital caliper (values were averaged after 3 measurements in different regions of the sample), and scaffolds were weighed using an analytical balance. Then, the apparent density of the ceramic part was determined geometrically. The total porosity of the scaffolds was then calculated from the apparent and theoretical (3.393 g·cm^{-3}) densities of hardystonite, as well as the open/closed porosity values.

The morphology of HT and HT-CS scaffolds was investigated in wet conditions by X-ray micro-tomography using a commercial tomograph, described in [39], equipped with a Varian paxscan detector (1920x1536 pixels) and a tungsten transmission X-ray source of 1-4 µm physical size. The lateral voxel size was set to 2 or 5 µm depending on the size of the sample.
Open porosity of HT scaffolds and pore interconnection size were measured by mercury intrusion porosimetry (MIP AutoPore IV, Micromeritics Ltd, Norcross, GA, USA).

X-ray diffraction (XRD) analyses at the external surfaces of HT and HT-CS scaffolds were performed using a D8 Advance diffractometer (CuKα, 40 kV, 40 mA) (Bruker AXS, Karlsruhe, Germany). Angular scans were acquired in a Bragg-Brentano θ-θ configuration, from 4° to 55° (2θ) with a step time of 129 s and a step size of 0.019° (2θ). Phase identification was carried out by comparison to standard patterns from the International Center for Diffraction Data – Powder Diffraction Files (ICDD-PDF) with the aid of DiffracPlus EVA software (Bruker). To identify the hardystonite phase, the PDF file #35-0745 was used. The obtained diffractograms were normalized with respect to the height of the peak of greatest intensity in the HT phase ((211) hardystonite peak at 31.1° (2θ)).

Some HT and HT-CS freeze dried scaffolds were broken in a three-points bending configuration to get access to clean fracture surfaces. Their microstructures were then analyzed on these fracture surfaces by scanning electron microscopy (SEM, Supra55VP (Zeiss, Germany) working at 1.5 kV) and optical stereo microscopy (Light Axiophot, Zeiss) in reflection mode. Prior to these analyses, scaffolds were freeze-dried to remove water without disturbing the hardystonite structure: they were frozen in a deep-freezer overnight then left for two days at -86 °C under 0.080 mbar absolute pressure for ice sublimation.

2.4. Rheology and Mechanical properties

Rheological measurements were conducted on chitosan solutions at 25 °C with shear rates ranging from 10^{-4} to 100 s^{-1}, using an AR2000 rheometer (TA Instruments, USA). The steady-state viscosity of chitosan solutions was assessed in static mode using a cone-plate geometry (aluminum set-up, 25 mm diameter, 4°). The minimum gap was fixed at 116 µm. A solvent trap was used to prevent evaporation of water during the measurements.

Compression tests of HT-CS scaffolds were performed using a mechanical universal testing machine (Instron 1121 UTM, Danvers, USA), at cross-head speed of 0.5 mm/min (strain rate about $3 \cdot 10^{-3}$ s^{-1}), at room temperature, and with the load axis orthogonal to the printing plane. At least ten samples were measured for each formulation (HT-CS-1 to HT-CS-5), and the results were reported as average ± standard deviation. The compression tests were performed in wet conditions for 3-D hardystonite scaffolds both before and after impregnation with CS hydrogel. Therefore, as a control, HT samples (before impregnation) were tested in water (they were labeled as "HT-H_2O" samples). Although the whole load-displacement curves were recorded for all samples, we focused on the analysis of a few criteria. The elastic part of the mechanical behavior was characterized by the apparent Young Modulus (E), maximum stress (σ_{max}), strain at maximum stress ($\varepsilon@\sigma_{max}$) and work at maximum stress ($W@\sigma_{max}$, calculated as the area under the stress-strain curve up to $\varepsilon@\sigma_{max}$). The dissipative part was characterized by comparing $W@\sigma_{max}$ to the work at 25% strain ($W@\varepsilon_{limit}$, calculated as the area under the stress-strain curve up to ε_{limit}, where ε_{limit} was arbitrarily chosen at 25%, out of the elastic part)[9].
Analysis of variance (ANOVA) was performed on the mechanical property data for the HT-CS and HT-H_2O samples, with $\alpha = 0.05$ (meaning that, for $p < 0.05$, at least one group of samples was statistically different compared with the other groups). To identify the sample or samples that was/were significantly different, a statistical study for each mechanical result was carried out using F-test followed by t-test.

3. Results

3.1. HT scaffold

XRD patterns acquired at the scaffolds surfaces are shown in Figure 1. Except for HT-CS-1 samples, the main characteristic planes corresponding to hardystonite (PDF file 35-0745) were identified: (111) at 2θ=23.928°, (201) at 2θ=28.910° and (211) at 2θ=31.130° for scaffolds before impregnation (HT) and after impregnation. Minor, secondary phases were detected in HT scaffolds, but could not be identified with full certainty: ZnO (PDF 36-1451), CaO (PDF 76-8925), $(Ca_{0.4}Zn_{0.6})O$ (PDF 76-8928), and potentially SiO_2 (cristobalite, PDF 85-0621), Ca_3Zn (PDF 41-0882) and K_2O (PDF 23-0493). Here, ZnO, CaO, $(Ca_{0.4}Zn_{0.6})O$ and Ca_3Zn probably come from some slight, local deviations from stoichiometry, while the presence of cristobalite might result from a very slight contamination by the milling media (Agate).
The micro, macro and total porosities of the HT scaffold structure were determined. The geometrical density of the HT scaffold was calculated from its external shape and its weight, leading to a total porosity of 72 vol%. A µ-CT reconstruction of HT scaffold structure is shown in Figure 2a. A regular macroporosity was observed, as well as indications that the filaments only slightly sag after printing. µ-CT displayed in Figure 2b shows that there was a very good adhesion between struts. No significant large porosity was present inside the struts. However, some longitudinal cracks were observed at the center of the filaments, mainly due to the volume contraction and CO_2 emission during the ceramization process [38]. Thus, further optimization of the ink composition and processing conditions is needed to completely eliminate these defects from the HT scaffolds. Apart from these cracks, only a small amount of intra-struts porosity (corresponding to the biggest defects) could be detected by µ-CT.

Table 1. Details of the impregnation protocols of HT scaffolds with chitosan solutions

Impregnation protocol	Impregnation Vacuum (mbar)	1st impregnation [CS_{1st}] wt%	2nd impregnation [CS_{2nd}] wt%	Gelation base (1M)	Sample name
1	50	0.5	2.5	NaOH	HT-CS-1
2	80	0.5	1.5	NH_4OH	HT-CS-2
3	50	0.5	1.5	NH_4OH	HT-CS-3
4	50	0.5	2.5	NH_4OH	HT-CS-4
5	50	1.5	1.5	NH_4OH	HT-CS-5

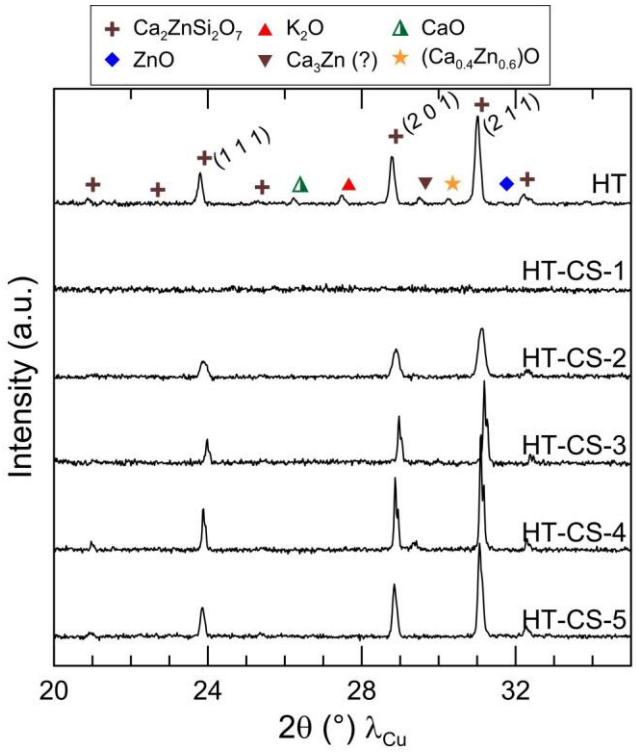

Figure 1: X-ray diffractograms of external surfaces of HT and HT-CS-x scaffolds (see Table 1 for sample numbers). The characteristic planes of hardystonite were identified: (111) at 2θ=23.928°, (201) at 2θ=28.910° and (211) at 2θ=31.130°. The background (contribution of water and amorphous phases to the diffraction signal) was subtracted from all diagrams, for the sake of clarity. The PDF cards used for identification were: hardystonite: 35-0745; ZnO: 36-1451; CaO: 76-8925; (Ca0.4Zn0.6)O: 76-8928; SiO2 (cristobalite): 85-0621; Ca3Zn 41-0882; K2O: 23-0493

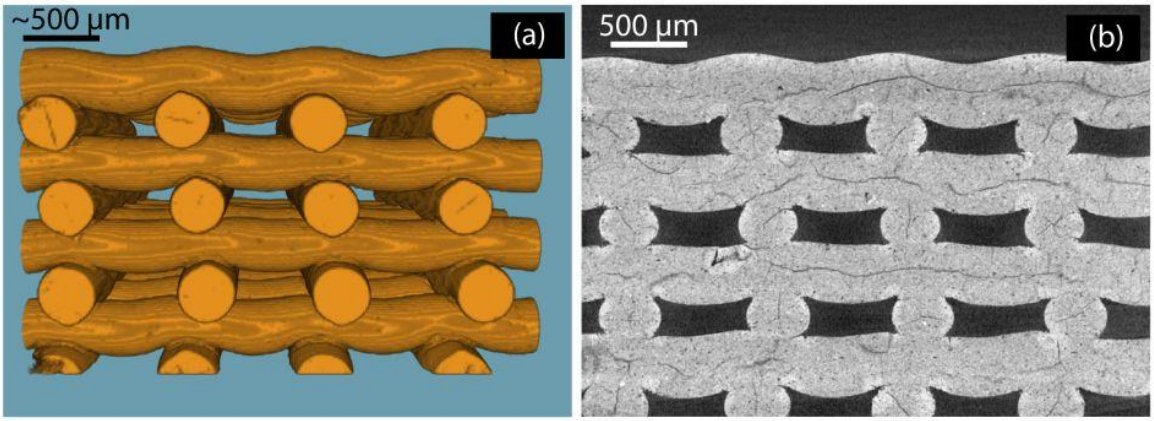

Figure 2: a) 3-D reconstruction and b) Cross-section of HT-scaffold obtained from µ-CT (lateral voxel size of 4 µm/voxel).

Mercury intrusion porosity (MIP) analysis, qualitatively confirmed by SEM micrographs (Figure 3), showed the presence of 0.1-1µm diameter micropores in the struts of the HT scaffolds. The total volume of micropores was 0.11 ± 0.01 mL/g, corresponding to a micro-porosity of the struts of 37 ± 5 vol.% (it will be referred to as "intra-strut porosity"). From this intra-strut porosity and the geometrical density, an inter-strut porosity of 61.5 ± 1.5 vol.% can be calculated.
Quite consistently with these calculations, the same inter-strut porosity measured by image analysis of X-ray tomograms was found to be around 58%. No information on inter-strut porosity morphology could be obtained from MIP, since the inter-strut pores were too large to be detectable by this technique.

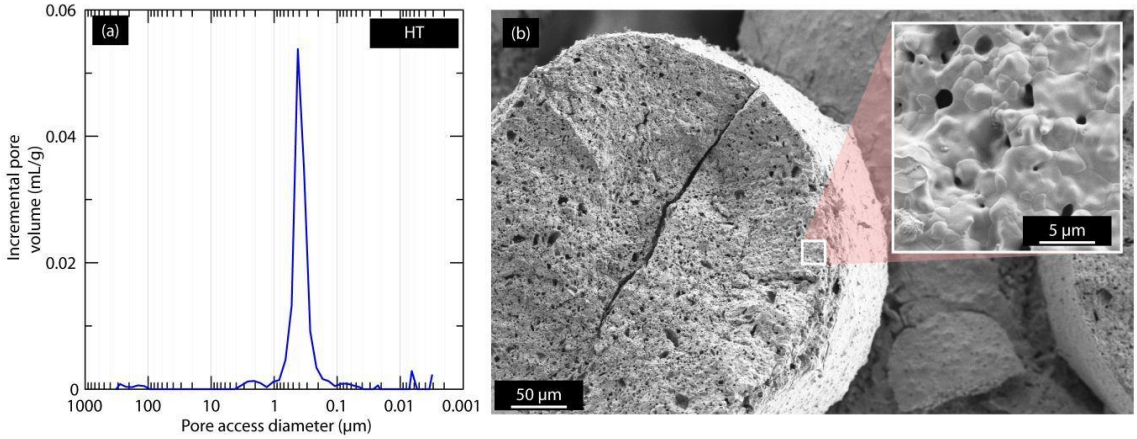

Figure 3: Mercury intrusion porosity of HT scaffold, showing a single family of pores with access diameter between 0.1 and 1 µm, and SEM picture of the same material, showing the pore size distribution.

3.2. Impregnation of HT scaffolds and formation of HT-CS scaffolds

The impregnation of the HT scaffolds by the CS solutions occurred by pressure gradient due to capillarity and to the applied vacuum. The chitosan aqueous solutions used for impregnations were all pseudo-plastic, shear-thinning fluids (Figure 4(a)), as previously reported [32,40]. Under these conditions, impregnation was expected to occur in the plateau region of the rheological curves, thus at low shear rates, in the range of Newtonian viscosity (Figure 4). The Newtonian viscosity of chitosan aqueous solution varied exponentially with chitosan concentration, with an apparently exponential increase in viscosity by 3 orders of magnitude between 0.5 wt% and 2.5 wt% chitosan solutions (from 0.8 ± 0.1 Pa·s to 1100 ± 120 Pa·s).
Table 2 shows the variations of the scaffold weights during the different steps of impregnation and gelation to form HT-CS scaffolds. Equations (1) to (8) (section 2.2) were used with the data reported in Table 2 to calculate the weight changes during the impregnation and gelation processes, the final chitosan concentration in the hydrogel impregnated in the scaffold and the CS/HT weight ratio (Table 3). Negative weight changes were measured during the gelation process, indicating losses of water during gelation.

Table 2: Weights of HT and HT-CS scaffolds at different stages of the impregnation process. Protocol numbers refer to Table 1 (n = 12).

Protocol	$m_0\ (g)$	$m_1(g)$	$m_2\ (g)$	$m_g\ (g)$
1	0.269 ± 0.015	0.507 ± 0.037	0.600 ± 0.133	0.588 ± 0.119
2	0.277 ± 0.015	0.541 ± 0.067	0.663 ± 0.082	0.561 ± 0.053
3	0.266 ± 0.022	0.530 ± 0.045	0.664 ± 0.064	0.564 ± 0.048
4	0.268 ± 0.022	0.521 ± 0.057	0.608 ± 0.075	0.544 ± 0.078
5	0.257 ± 0.026	0.712 ± 0.102	0.748 ± 0.078	0.626 ± 0.068

Table 3. Changes in weight for HT and HT-CS scaffolds, final chitosan concentration in HT scaffold and CS/HT ratio. Protocol numbers refer to Table 1 (n = 12).

Protocol	m_{sol}^{1-0} (g)	m_{sol}^{2-1} (g)	m_{sol}^{g-2} (g)	m_{CS}^{1-0} (g)	m_{CS}^{2-1} (g)	$[CS_r]$ $wt\%$	m_{CS}^{g-2} (g)	CS/HT
1	0.238 ± 0.022	0.093 ± 0.096	-0.012 ± 0.014	0.119 ± 0.011	0.233 ± 0.240	0.907 ± 0.432	-0.005 ± 0.007	1.239 ± 0.892
2	0.264 ± 0.052	0.122 ± 0.015	-0.102 ± 0.029	0.132 ± 0.026	0.183 ± 0.022	0.819 ± 0.016	-0.083 ± 0.022	0.826 ± 0.210
3	0.264 ± 0.023	0.134 ± 0.019	-0.100 ± 0.016	0.132 ± 0.012	0.201 ± 0.028	0.835 ± 0.012	-0.083 ± 0.012	0.929 ± 0.119
4	0.253 ± 0.035	0.087 ± 0.018	-0.064 ± 0.003	0.127 ± 0.018	0.218 ± 0.045	1.008 ± 0.027	-0.064 ± 0.001	1.031 ± 0.153
5	0.455 ± 0.076	0.036 ± 0.024	-0.122 ± 0.010	0.683 ± 0.114	0.054 ± 0.036	1.500 ± 0.000	-0.183 ± 0.015	2.110 ± 0.429

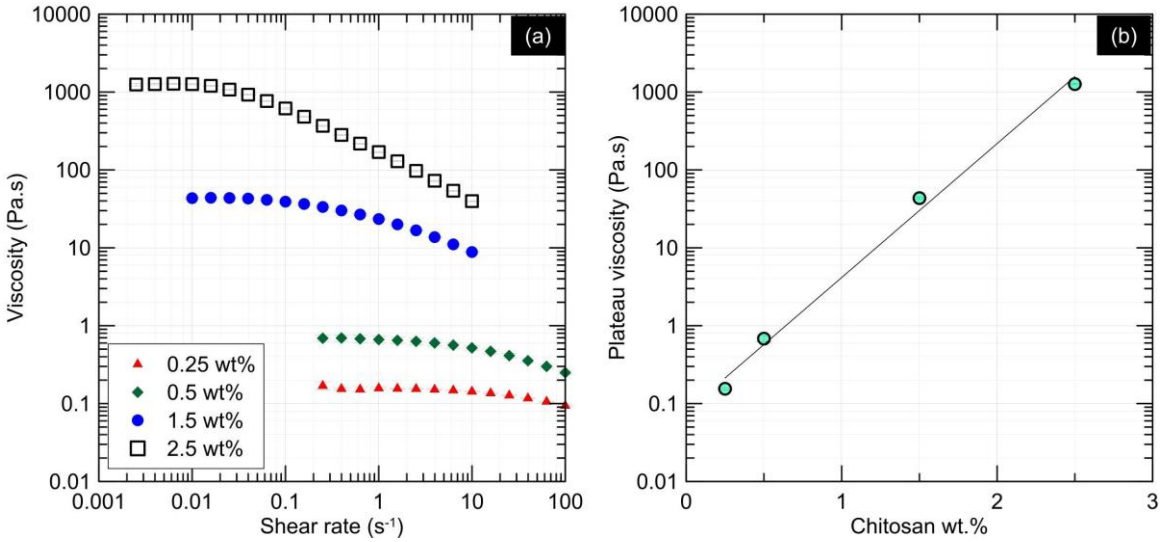

Figure 4: (a) Rheological measurements on chitosan solutions. Tests conducted at shear rates between 10-4 or 10-3 s-1 and 100 s-1 at 25°C). (b) Exponential increase in plateau viscosity with chitosan concentration.

3.3. Characterization of HT-CS scaffolds

Once the scaffolds were impregnated, the external surfaces were analyzed by XRD to investigate the effect of chitosan on composition and phase stability. Figure 1 shows the diffractograms for HT before and after impregnation following all protocols. It was observed that the characteristic planes of hardystonite were identified in all cases, (111) at 2θ=23.928°, (201) at 2θ=28.910° and (211) at 2θ=31.130°, except in HT-CS-1, the only one sample in which a sodium hydroxide solution was used to induce gelation. It is also observed that, whatever the impregnation protocol, no chitosan peak was detected (indicating that, if present, the crystallinity of chitosan remained below the detection limit, thus most (or all) of the chitosan was amorphous). Besides, since the XRD analyses were performed on non-flat surfaces, artifacts such as peak splitting or peak widening were observed for all samples.

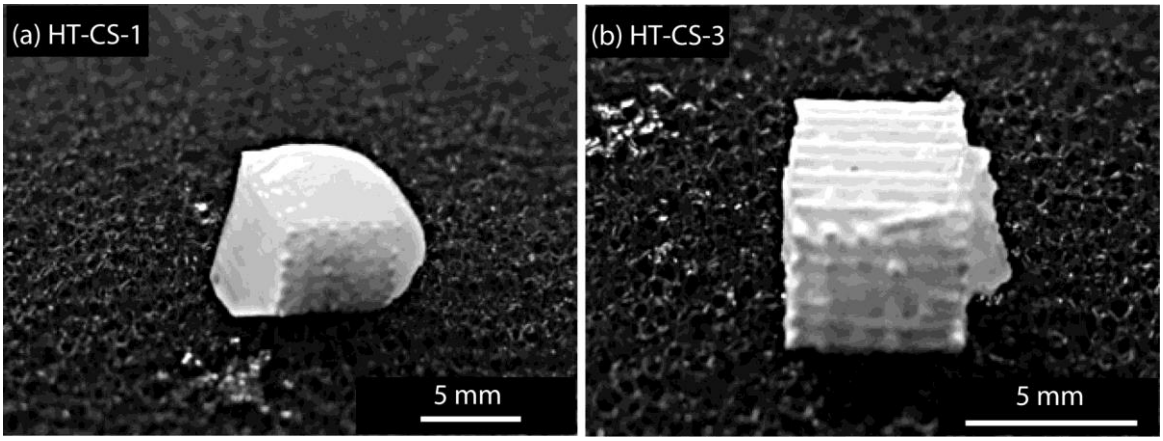

Figure 5: Pictures of HT-CS-1 and HT-CS-3 scaffolds.

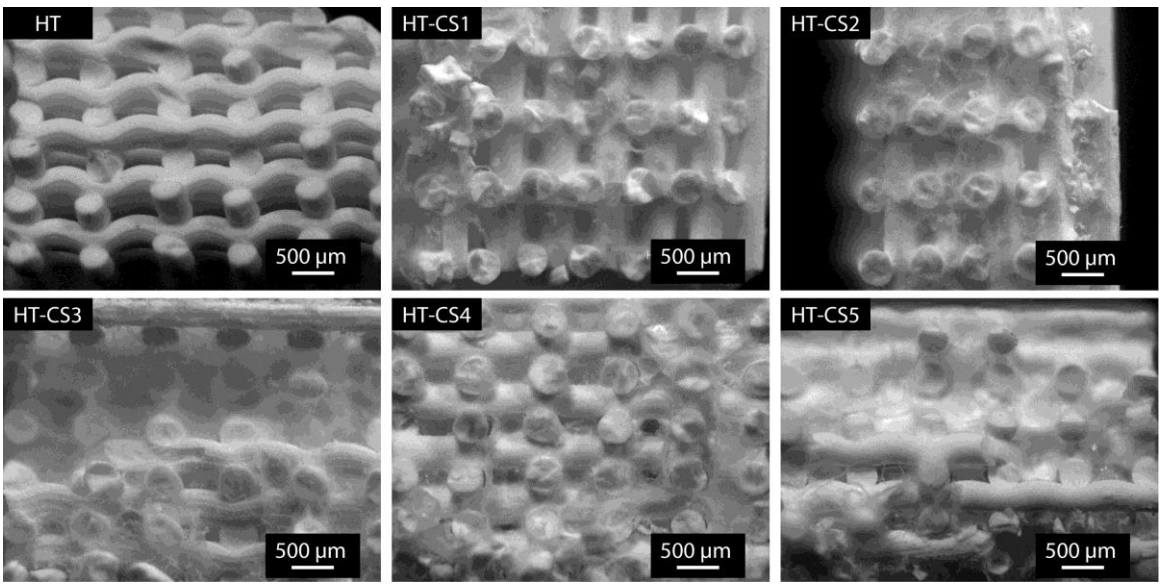

Figure 6: Optical microscopy micrographs of bending fracture surface of HT and HT-CS-x scaffolds (x as defined in Table 1).

Figure 5(a) (fracture surface of HT-CS-1 sample) shows the dense chitosan physical hydrogel covering the surface of a HT scaffold after its impregnation. Additionally, a picture of the fracture surface of sample HT-CS-3 is shown as an example of HT-CS scaffolds gelled by ammonia vapors (Figure 5(b)).

Optical micrographs of fracture surface of freeze-dried scaffolds are reported in Figure 6, before (HT) and after (HT-CS scaffolds) impregnation. There was a clear difference between HT and HT-CS scaffolds: chitosan appeared as a continuous phase homogeneously filling the macropores of HT-CS, under all impregnation conditions.

SEM observations enabled analyzing the presence of chitosan in the strut microporosity for different impregnation protocols. In particular, Figure 7 and Figure 8 show cross section of struts (left – (a), (b), (c) – in figures 7 and 8) and micropores (right – (d), (e), (f) – in figures 7 and 8). Coherently with µ-CT observations (Figure 2), the presence of longitudinal cracks in the ceramic phase (due to contraction during ceramization) is confirmed. A layer of chitosan was observed covering the surface of the struts and, at the micrometer scale, chitosan was partially filling the largest micropores of HT-CS scaffolds.

The presence of chitosan in the struts microporosity for different HT-CS scaffolds in the wet state could not be evidenced by μ-CT (X-ray tomography), probably because of the absence of contrast in X-rays absorption between water and chitosan.

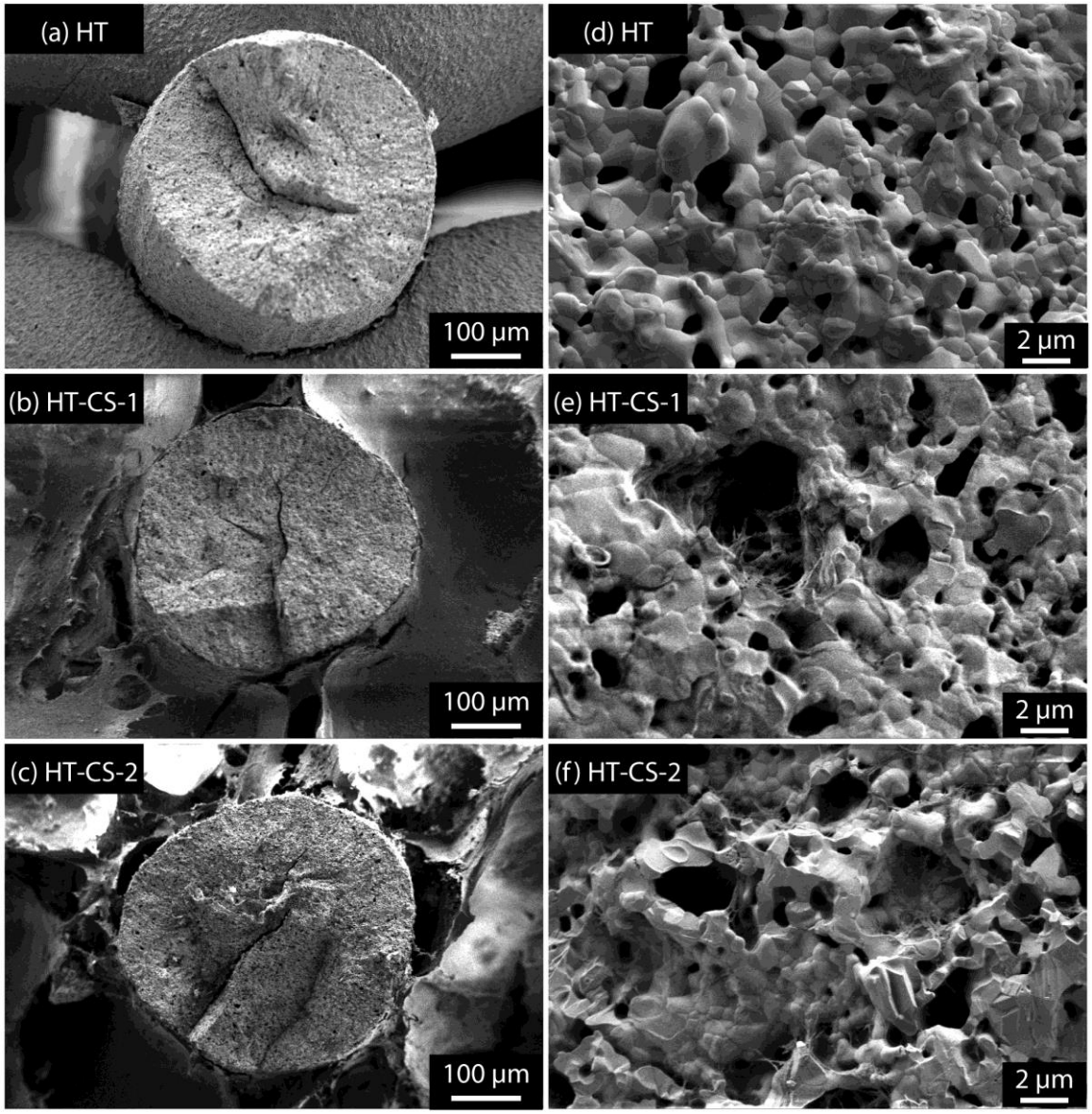

Figure 7: Secondary electron SEM micrographs of HT, HT-CS-1 and HT-CS-2 scaffolds. Column a: cross section of struts; column b: detail of the fracture surface of struts.

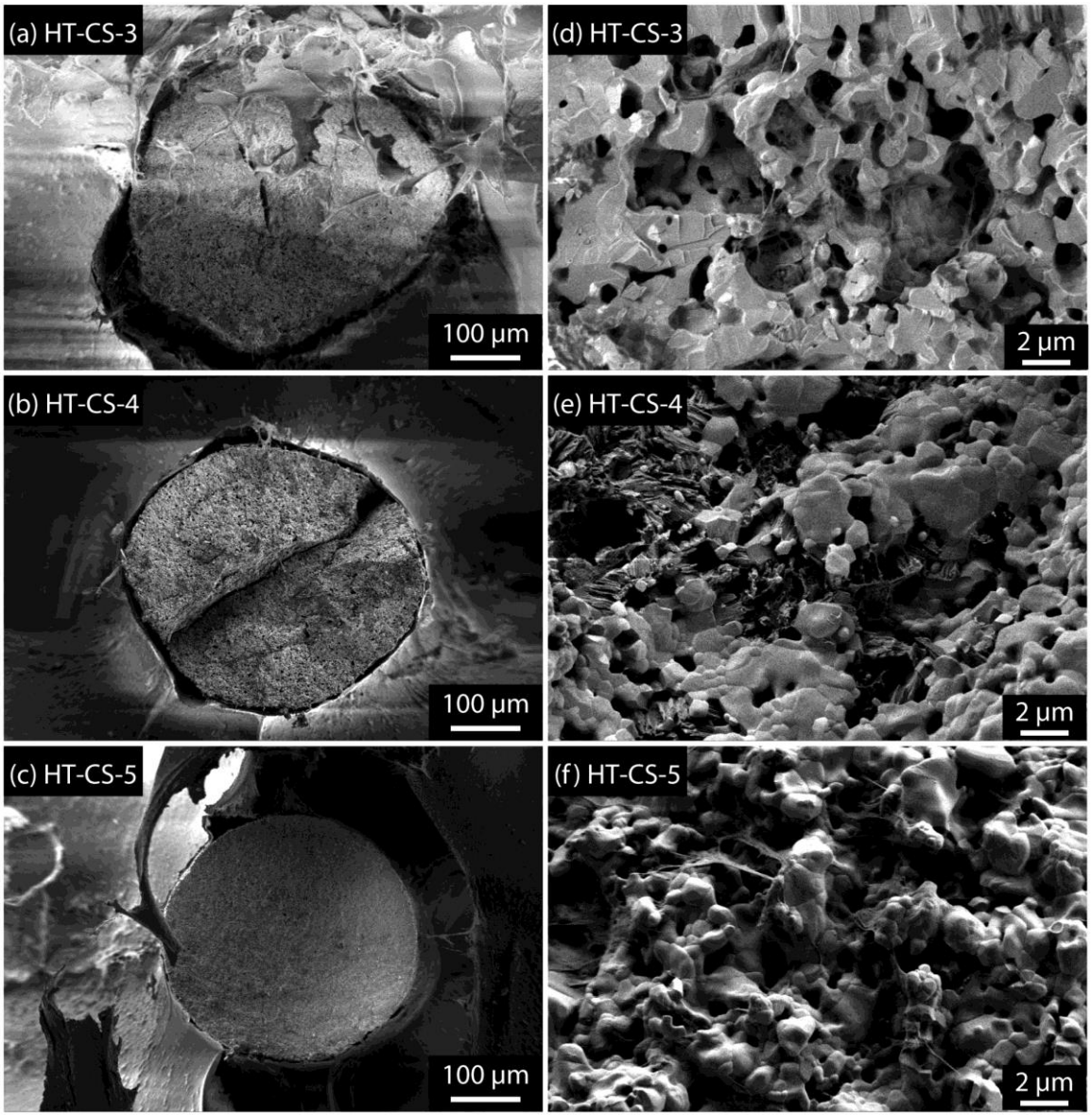

Figure 8: SEM micrographs of HT-CS-3 to HT-CS-5 scaffolds. Column a: cross section of struts; column b: detail of the fracture surface of struts.

Table 4. Analysis of stress - strain data for HT-H_2O and HT-CS-x scaffolds (as-defined in Table 1), and CS/HT ratio ($n \geq 10$).

Sample	Max stress (MPa)	Strain at max stress (%)	Work at max stress (%MPa)	Apparent Young's modulus (MPa)	Work at limit strain (25%) (%MPa)	CS/HT ratio
	σ_{max}	$\varepsilon@\sigma_{max}$	$W@\sigma_{max}$	E	$W@\varepsilon_{limit}$	
HT-H_2O	3.28 ± 1.14	7.66 ± 4.16	9.39 ± 6.10	228.47 ± 118.65	19.30 ± 10.62	
HT-CS-1	4.18 ± 1.19	9.53 ± 1.13	13.46 ± 3.84	187.78 ± 90.60	38.13 ± 9.99	1.24 ± 0.89
HT-CS-2	2.86 ± 0.89	8.00 ± 0.65	9.15 ± 2.42	134.33 ± 44.25	24.74 ± 5.45	0.83 ± 0.21
HT-CS-3	3.02 ± 0.67	8.12 ± 0.70	9.74 ± 2.12	148.68 ± 55.74	29.52 ± 4.35	0.93 ± 0.12
HT-CS-4	3.57 ± 0.71	9.07 ± 0.93	11.68 ± 2.00	171.17 ± 37.54	33.25 ± 5.60	1.03 ± 0.15
HT-CS-5	4.26 ± 1.43	27.24 ± 9.86	54.39 ± 28.59	99.02 ± 1.85	41.53 ± 8.25	2.11 ± 0.43

Analysis of stress-strain data of HT-CS in the wet state and HT-H_2O (Figure 9 and Table 4) enabled an estimation of the effect of CS/HT ratio on mechanical properties such as maximum stress, the corresponding strain at maximum stress, the work at maximum stress, the apparent Young´s modulus and the work at limit strain of 25% (all these parameters are schematized in Figure 9 (b)).

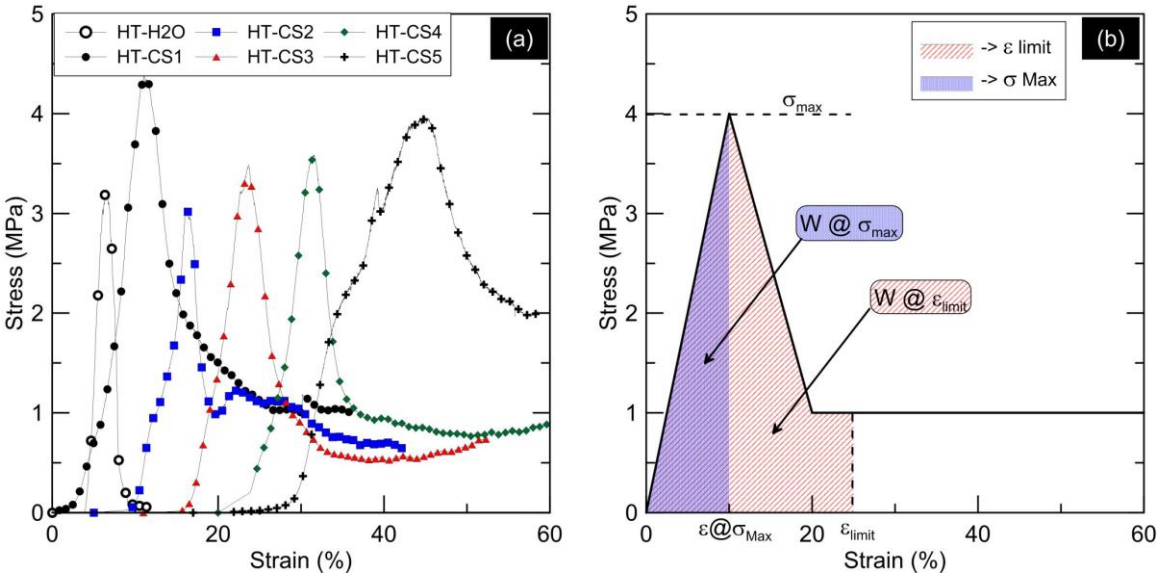

Figure 9: (a): Stress vs. strain curves for HT-H2O and HT-CS scaffolds. For clarity purpose, curves are stacked with offsets along the strain axis. (b): Schematic representation of the analysis performed on stress-strain curves of each sample. Maximum stress: σmax; strain at maximum stress: ε@σmax; work at maximum stress: W@σmax; apparent Young´s modulus: E; and work at limit strain: W@εlimit.

4. Discussion

In the HT-CS scaffolds, the CS/HT weight ratio ranged from 0.83 to 2.11. In the lyophilized systems, chitosan appeared as a film around the struts and inside the struts microporosity (Figure 7 and 8).

4.1. Impregnation of HT scaffolds

Considering the microporosity (intra-strut porosity) of 41 vol%, with pore access diameters from 0.1 to 1 µm, and the inter-strut porosity of ~60 vol%, impregnation of HT scaffolds may be considered as a case of liquid transport in porous solid by mechanisms of ordinary diffusion governed by the Darcy equation (equation 9) and viscous flow governed by the Hagen-Poiseuille equation (equation 10).

$$v_0 = -\frac{\kappa}{\mu}\frac{dP}{dL} \tag{9}$$

In equation 9, v_0 is the superficial velocity ($v_0 = \frac{Q}{\pi R^2}$); κ is the permeability of porous medium; P is the pressure and L is the length of the pore.

$$\Delta P = \frac{8\mu L Q}{\pi R^4} \tag{10}$$

In equation 10, ΔP is the pressure difference between the two ends, μ is the dynamic viscosity, Q is the volumetric flow rate; R is the pore radius; and L is the length of the pore.

According to Darcy and Hagen-Poiseuille equations, the impregnation velocity should increase with applied pressure and decrease with the CS solution viscosity. Here, ΔP was estimated as the sum of Laplace's capillary pressure (ΔP_L in equation 11) and atmospheric pressure (with atmospheric pressure equal to 1 bar, it was considered that a variation in impregnation vacuum from 50 to 80 mbar did not significantly impact ΔP).

$$\Delta P_L = \frac{2\gamma cos\theta}{R} \quad (11)$$

In equation 11, γ is the surface tension of the solution; θ is the contact angle and R the capillary radius. As a first, rough approximation, the surface tension and contact angles of the CS solutions were considered equal to those of pure water (surface tension of $72 \cdot 10^{-3}$ N·m^{-1} at room temperature, contact angle of water on hardystonite of ~33° [41]). Although the presence of adsorbed chitosan could change the contact angle, it was considered that the global impact of this approximation on the orders of magnitude involved here was minimal.
With these considerations, the order of magnitude of the maximum viscosity (μ) that enabled impregnation of the CS solutions in the micropores and and in the inter-strut porosity could be estimated.
Taking into account Laplace's capillary pressure only, a viscosity lower than ~$4 \cdot 10^3$ Pa·s was necessary for the solution to effectively flow through the micropores of the HT scaffolds and reach the center of the struts. When taking into account only the atmospheric pressure, the viscosity should be lower than ~10^3 Pa·s. When taking into account the sum of the two aforementioned pressures, the viscosity should be below ~$5 \cdot 10^3$ Pa·s. Based on the rheological curves of the chitosan solutions used for impregnation of HT scaffolds (Figure 4), all Newtonian (plateau) viscosities were lower than these estimations. As a result, all CS solutions could flow into the micropores of HT scaffolds.
However, to fully impregnate the microporosity, the inter-strut porosity should also be impregnated by the chitosan solution, and as little gas as possible should remain inside the micropores. In order for the CS solution to flow through the inter-strut porosity until the center of the sample, its viscosity should be lower than ~$2 \cdot 10^2$, ~$2 \cdot 10^4$ and ~$2 \cdot 10^4$ when taking into account only the capillary pressure, only the atmospheric pressure and the sum of these two pressures, respectively, showing that in this case the capillary pressure is negligible. For the case of chitosan solutions at 0.5 and 1.5 wt% (viscosity of ~1 and ~50 Pa·s, respectively), impregnation could occur by capillarity, whereas capillary pressure was not high enough to impregnate the inter-strut porosity of a HT scaffold with a 2.5 wt% CS solution (10^3 Pa·s). This indicates that applying vacuum prior impregnation was necessary not only to take out the air bubbles from the scaffolds, but also to increase ΔP so as to completely impregnate the HT scaffold when using a 2.5 wt% chitosan solution.

Consequently, for the case of impregnation of HT scaffolds using different protocols (Table 1), the weight of chitosan gained during scaffold impregnation was expected to depend on the concentration and viscosity of the chitosan solution and on the degree of impregnation vacuum. As the chitosan concentration increases, the amount of impregnated chitosan should increase. As the viscosity of chitosan solution increases, the amount of impregnated solution should decrease. It was also expected that the amount of impregnated solution would be higher with an impregnation vacuum of 50 mbar instead of 80 mbar. In these regards, some trends derived from data reported in Table 1 are discussed below.

1. Effect of chitosan solution concentration

Protocols 3 and 4 only differed in the concentration of the chitosan solution used during the second impregnation (1.5 wt.% for protocol 3, 2.5 wt.% for protocol 4, see Table 1). As expected, the same gains in the amount of the chitosan solution ($m_{sol}{}^{1-0}$) and of the chitosan solute weights ($m_{CS}{}^{1-0}$) were measured after the first impregnation for both protocols (Table 3). However, after the second

impregnation the gain in solution weight (${m_{sol}}^{2-1}$) was 1.5 times higher in protocol 3 than in protocol 4 but, due to the higher concentration used in protocol 4, the gain in chitosan weight (${m_{CS}}^{2-1}$) was about identical. This could be explained considering that, at lower chitosan concentration (i.e., in protocol 3), the viscosity was lower (Figure 4). This facilitated the impregnation of the inter-strut porosity (the only one reachable after the first impregnation) that is more sensitive to the viscosity of the impregnation solution, as discussed above. Thus, the weight of impregnated solution was higher, as expected by liquid diffusion laws. However this just about equilibrated the lower CS concentration in the solution, to result in a similar gain in CS weight for both protocols 3 and 4.

Protocols 3 and 5 used the same impregnation vacuum; the concentration of chitosan was higher in protocol 5 (1.5 wt.% *vs* 0.5 wt.% for protocol 3) for the first impregnation but was the same one (1.5 wt.%) in both protocols for the second impregnation (Table 1). During the first impregnation, as shown in Table 3, weight gains were significantly higher for protocol 5 (1.7 times for weight of solution (${m_{sol}}^{1-0}$) and 5.2 times for weight of chitosan (${m_{CS}}^{1-0}$)). Although the viscosity was higher in protocol 5, the dominant effect was the high concentration of chitosan (thrice higher than the concentration used in protocol 3). On the contrary, during the second impregnation, the weight gain for protocol 3 was higher: 3.7 times for both the weight of solution (${m_{sol}}^{2-1}$) and the weight of chitosan (${m_{CS}}^{2-1}$). To explain these results, it should be considered that the viscosity of the solution already impregnating the scaffolds (after 1st impregnation) was higher for protocol 5 than for protocol 3. Therefore, resistance for further impregnation was higher in protocol 5. As a result of both impregnations, HT-CS-5 contained more chitosan than HT-CS-3, highlighting the beneficial effect of a first impregnation with a higher CS concentration.

2. Effect of impregnation vacuum

Protocols 2 and 3 only differed in the impregnation vacuum: 80 mbar for protocol 2 and 50 mbar for protocol 3 (Table 1). During the first impregnation (with a 0.5 wt.% CS solution), the resulting weight increase was in the same range, 95% in both cases. In the second impregnation (with a 1.5 wt.% CS solution), a slightly higher, but not significantly different, amount of weight was gained in protocol 3. This small difference was reflected in a slightly higher CS/HT weight ratio (1.1 times) in the final samples obtained with protocol 3 (Table 3). This indicates that the pressure has only a weak effect on impregnation, at least in the ranges of pressures and chitosan concentrations studied here.

3. Effect of the nature of the base used for gelation

Protocols 1 and 4 differed only in the base used for gelation, sodium hydroxide for protocol 1 and vapors of ammonia for protocol 4 (Table 1). During gelation, sample processed with protocol 4 lost more than 10% of the weight of the already impregnated CS solution, while the weight of the sample under protocol 1 remained constant (Table 3).

Gelation depends upon availability of hydroxyl anions, which are provided by the base. Sodium hydroxide is a strong base that rapidly and completely dissociates in solution, forming sodium cations and hydroxyl anions. Ammonia vapors first dissolve in the acidic chitosan aqueous solution. Then, ammonia being a weak base, it partially dissociates forming ammonium cations and hydroxyl anions. Under these conditions, hydroxyl anions were available more rapidly for gelation using sodium hydroxide solution than using ammonia vapors. Thus, in the case of gelation induced by sodium hydroxide, the diffusion of the base and the neutralization were fast, resulting in CS hydrogel being "frozen" in a structural state close to the one of the solution. When gelled with ammonia vapor, the CS solutions had more time to evolve towards a more equilibrated, compact structural state. As a result, more syneresis occurred during gelation with ammonia, hence the larger water loss. Another mechanism can also explain the smaller weight loss when performing the gelation with NaOH: as diffusion of the base and neutralization were faster as compared to gelation induced by ammonia vapors, almost instantaneous formation of an opaque layer was observed. This opaque layer was also observed with ammonia vapors, but after much longer times (difference of

~10 minutes). This layer constituted a mass transfer resistance for the solution to flow out of the samples during gelation, but did not prevent the overall gelation process to be faster with NaOH. Considering the first mechanism, weight loss would be due to loss of water. With the second mechanism, the weight loss would be due to the loss of CS solution (and equations (7) and (8) are coherent with the second mechanism).

4.2. Architecture and microstructure of scaffolds

The inter-strut porosity was both calculated from mercury intrusion porosimetry and measured by µ-CT, with rather close results (61.5 ±1.5 and 58 vol% respectively). This small difference can be ascribed to two factors: imprecision of the geometrical density (needed to recalculate the inter-strut porosity by MIP), and doubts on how the cracks (Figure 2(b)) are taken into account in MIP measurements (to what extent they are accessible by mercury is unknown). The designed porosity in the CAD file was ~55 vol%, which is rather close to the µCT measurement (58%), that should however not be taken as an absolutely perfect measure. Indeed, image processing and analysis can lead to some measurement errors. It is also probable that since the struts were subjected to limited sagging during printing, this slight change of the overall shape can lead to minor divergence of the experimentally measured inter-strut porosity value from the one defined by the CAD model.
XRD of HT-CS surfaces showed well-defined crystalline structures of pure hardystonite, except for HT-CS-1 (Figure 1). The unexpected result in the case of HT-CS-1, in which neither chitosan nor hardystonite peaks were detected in the diffractogram, could be explained by the layer of chitosan hydrogel covering the surface (Figure 5(a)), thick enough to screen the crystal structure in XRD analysis. In fact, to the naked eye, this layer was more opaque and thicker than for scaffolds in which ammonia vapors were used as a base for gelation (Figure 5). This was completely consistent with the fact that, as previously discussed, the final CS/HT weight ratio was higher for the sample gelled with NaOH than for the samples gelled with ammonia vapors (Protocols 1 *vs.* 4, Table 3).
Layers of chitosan covering the fracture surface and filling the macropores of HT-CS scaffolds were observed by optical microscopy and by SEM (Figure 6, Figure 7 and Figure 8). Observation of the fracture surface of HT scaffold by SEM enabled identifying a significant number of empty micropores (Figure 7(d)). In contrast, those empty micropores were rarely found in the fracture surface of sample HT-CS-5 (Figure 8(f)), that corresponded to the scaffold with the highest amount of chitosan, i.e. with a final CS/HT weight ratio higher than 2 (Table 3). Observation of micropores at fracture surfaces showed chitosan filaments that filled and bridged micropores, in contrast with HT scaffold where no filaments were observed (Figure 7(d,e,f) and 8(d,e,f)). Moreover, the frequency of those CS filaments increased with the content in chitosan, whereas the numbers of visible micropores decreased from HT-CS-2 to HT-CS-5.

4.3. Mechanical properties

Experimental results of mechanical properties (Table 4) were analyzed by ANOVA (see section 2.4) with respect to variables in the impregnation procedure (Table 1) and the final chitosan content (CS/HT ratio, Table 3). Due to a large variability intrinsic to porous ceramics, the analysis of mechanical properties hardly showed significant differences when directly comparing materials. However, some trends could be highlighted with reasonable accuracy, as summarized in Figure 10. In particular, increases with increasing CS/HT ratio were detected in the strain at maximum stress, the work at limit strain and the work at maximum stress.

On the other hand, some other mechanical properties were not impacted by the impregnation with the CS solution. Considering the maximum stress, none of the HT-CS samples exhibited a statistically significant difference from the HT-H_2O samples ($p > 0.05$). This indicates that the chitosan content did not impact the maximum stress of the HT-CS samples; therefore, compressive strength should mainly be attributed to the hardystonite ceramic. Considering the apparent Young's modulus, all HT-CS samples showed a lower mean Young's modulus compared with HT-H_2O samples; however, only the HT-CS-2, HT-CS-3 and HT-CS-5 samples were statistically different

from HT-H_2O samples (p values were ~0.01, ~0.04 and ~0.001 in t-test respectively). Nevertheless, even if these differences were statistically significant, there were too many experimental biases (not reflected in the statistics) to validate a change in the Young's modulus with CS/HT ratio (in particular, as the modulus was measured at the maximum of the stress-strain compression curve, without any loading-unloading cycles, it may have been underestimated in all materials).
No visible effect on the mechanical properties of the base used for gelation or of the impregnation vacuum level (HT-CS-1 *vs.* HT-CS-4 and HT-CS-2 *vs.* HT-CS-3 respectively) could be detected.

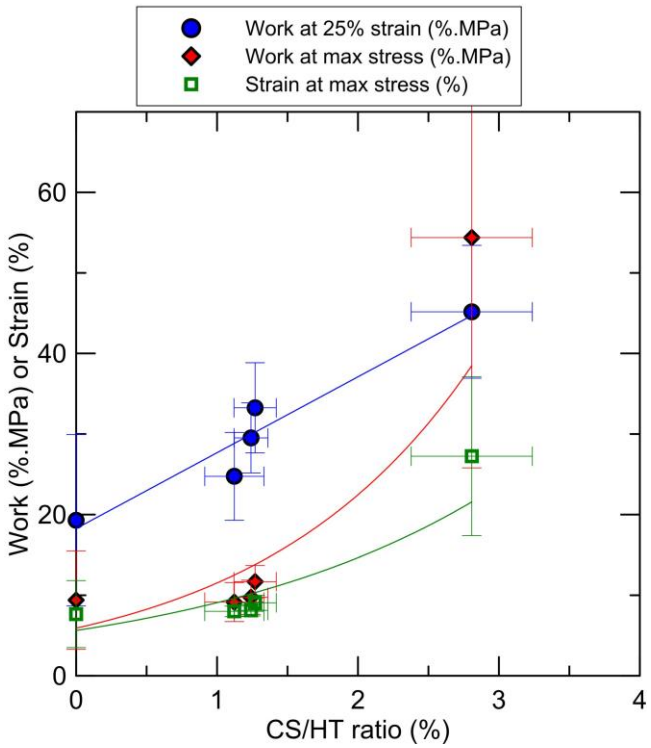

Figure 10: Evolution of the mechanical properties with CS/HT ratio (n ≥ 10).

5. Conclusions

HT and HT-CS scaffolds fabricated in this work showed a well-defined ceramic crystalline structure corresponding to hardystonite with some very minor secondary phases, as revealed by XRD. HT scaffolds possessed both macro- and micro-porosities, which made these 3-D structures suitable for impregnation with chitosan solutions (with concentration ranging from 0.5 wt% to 2.5 wt%). After two subsequent impregnations, chitosan was observed to be present within the different pores in the structure of the samples (intra- and inter-struts porosity).
HT-scaffolds gained some weight during impregnation, depending on two related variables of the chitosan solution: its concentration and viscosity. As a result, the maximum chitosan/hardystonite ratio (2.11) was obtained using the highest CS solution concentration during the first impregnation. The rate of gelation seemed to affect the resistance to mass transfer during the second impregnation, due to the formation of a dense surface layer. When sodium hydroxide was used for gelation, the rate of gelation was higher; consequently, the weight loss experienced during gelation was lower.
In HT-CS scaffolds (hardystonite scaffolds impregnated with a CS hydrogel), the capacity for energy dissipation and for load bearing tended to increase with increasing amount of impregnated chitosan. The specific impregnation conditions affected the mechanical properties: a higher chitosan content improved the energy dissipation during fracture of HT-CS scaffolds; the base used for gelation affected the weight loss during gelation, but no statistically significant effect was found on the mechanical properties.
Moreover, chitosan filaments bridged the cracks, and therefore might contribute to the improvement of the stiffness and energy dissipation of the HT-CS scaffolds.

6. Acknowledgments

This work was supported by the LABEX iMUST (ANR-10-LABX-0064) of Université de Lyon, within the program "Investissements d'Avenir" (ANR-11-IDEX-0007) operated by the French National Research Agency (ANR).

7. References

1. Wright, N.C., Looker, A.C., Saag, K.G., Curtis, J.R., Delzell, E.S., Randall, S., & Dawson-Hughes, B. (2014). The Recent Prevalence of Osteoporosis and Low Bone Mass in the United States Based on Bone Mineral Density at the Femoral Neck or Lumbar Spine, *Journal of Bone and Mineral Research, 29 (11)*, 2520-2526. Doi: 10.1002/jbmr.2269
2. Amini, A. R., Laurencin, C. T., & Nukavarapu, S. P. (2012). Bone Tissue Engineering: Recent Advances and Challenges. *Critical Reviews™ in Biomedical Engineering*, *40*(5). doi:10.1615/CritRevBiomedEng.v40.i5.10
3. Philippart, A., Boccaccini, A. R., Fleck, C., Schubert, D. W., & Roether, J. A. (2015). Toughening and functionalization of bioactive ceramic and glass bone scaffolds by biopolymer coatings and infiltration: a review of the last 5 years. *Expert Review of Medical Devices*, *12*(1), 93–111. doi:10.1586/17434440.2015.958075
4. Bianco, A., Di Federico, E., & Cacciotti, I. (2011). Electrospun poly(ε-caprolactone)-based composites using synthesized β-tricalcium phosphate. *Polymers for advanced technology , 22[12]*, 1832-1841. Doi: 10.1002/pat.1680
5. Komlev, V. S., Barinov, S. M., & Rustichelli, F. (2003). Strength enhancement of porous hydroxyapatite ceramics by polymer impregnation. *Journal of Materials Science Letters*, *22*(17), 1215–1217. doi:10.1023/A:1025300617681
6. Martínez-Vázquez, F. J., Perera, F. H., Miranda, P., Pajares, A., & Guiberteau, F. (2010). Improving the compressive strength of bioceramic robocast scaffolds by polymer infiltration. *Acta Biomaterialia*, *6*(11), 4361–4368. doi:10.1016/j.actbio.2010.05.024
7. Miao, X., Lim, W.-K., Huang, X., & Chen, Y. (2005). Preparation and characterization of interpenetrating phased TCP/HA/PLGA composites. *Materials Letters*, *59*(29), 4000–4005. doi:10.1016/j.matlet.2005.07.062
8. Miao, X., Tan, D. M., Li, J., Xiao, Y., & Crawford, R. (2008). Mechanical and biological properties of hydroxyapatite/tricalcium phosphate scaffolds coated with poly(lactic-co-glycolic acid). *Acta Biomaterialia*, *4*(3), 638–645. doi:10.1016/j.actbio.2007.10.006
9. Peroglio, M., Gremillard, L., Chevalier, J., Chazeau, L., Gauthier, C., & Hamaide, T. (2007). Toughening of bio-ceramics scaffolds by polymer coating. *Journal of the European Ceramic Society*, *27*(7), 2679–2685. doi:10.1016/j.jeurceramsoc.2006.10.016
10. Peroglio, M., Gremillard, L., Gauthier, C., Chazeau, L., Verrier, S., Alini, M., & Chevalier, J. (2010). Mechanical properties and cytocompatibility of poly(ε-caprolactone)-infiltrated biphasic calcium phosphate scaffolds with bimodal pore distribution. *Acta Biomaterialia*, *6*(11), 4369–4379. doi:10.1016/j.actbio.2010.05.022
11. Li, J., & Kao, W. J. (2003). Synthesis of polyethylene glycol (PEG) derivatives and PEGylated-peptide biopolymer conjugates. *Biomacromolecules*, *4*(4), 1055–1067. doi:10.1021/bm034069l
12. Hersel, U., Dahmen, C., & Kessler, H. (2003). RGD modified polymers: biomaterials for stimulated cell adhesion and beyond. *Biomaterials*, *24*(24), 4385–4415.
13. Lu, H., Kawazoe, N., Tateishi, T., Chen, G., Jin, X., & Chang, J. (2010). In vitro proliferation and osteogenic differentiation of human bone marrow-derived mesenchymal stem cells cultured with hardystonite (Ca2ZnSi2O7) and {beta}-TCP ceramics. *Journal of Biomaterials Applications*, *25*(1), 39–56. doi:10.1177/0885328209342469
14. Elsayed, H., Zocca, A., Franchin, G., Bernardo, E., & Colombo, P. (2016). Hardystonite bioceramics from preceramic polymers. *Journal of the European Ceramic Society*, *36*(3), 829–835. doi:10.1016/j.jeurceramsoc.2015.10.034

15. Ramaswamy, Y., Wu, C., Zhou, H., & Zreiqat, H. (2008). Biological response of human bone cells to zinc-modified Ca-Si-based ceramics. *Acta Biomaterialia*, *4*(5), 1487–1497. doi:10.1016/j.actbio.2008.04.014
16. Wu, C., Chang, J., & Zhai, W. (2005). A novel hardystonite bioceramic: preparation and characteristics. *Ceramics International*, *31*(1), 27–31. doi:10.1016/j.ceramint.2004.02.008
17. Zhang, M., Lin, K., & Chang, J. (2012). Preparation and characterization of Sr–hardystonite (Sr2ZnSi2O7) for bone repair applications. *Materials Science and Engineering: C*, *32*(2), 184–188. doi:10.1016/j.msec.2011.10.017
18. Studart, A. R., Gonzenbach, U. T., Tervoort, E., & Gauckler, L. J. (2006). Processing Routes to Macroporous Ceramics: A Review. *Journal of the American Ceramic Society*, *89*(6), 1771–1789. doi:10.1111/j.1551-2916.2006.01044.x
19. Jaiswal, A. K., Chhabra, H., Kadam, S. S., Londhe, K., Soni, V. P., & Bellare, J. R. (2013). Hardystonite improves biocompatibility and strength of electrospun polycaprolactone nanofibers over hydroxyapatite: A comparative study. *Materials Science and Engineering: C*, *33*(5), 2926–2936. doi:10.1016/j.msec.2013.03.020
20. Lin, K., Zhai, W., Ni, S., Chang, J., Zeng, Y., & Qian, W. (2005). Study of the mechanical property and in vitro biocompatibility of CaSiO3 ceramics. *Ceramics International*, *31*(2), 323–326. doi:10.1016/j.ceramint.2004.05.023
21. Shahidi, F., & Abuzaytoun, R. (2005). Chitin, chitosan, and co-products: chemistry, production, applications, and health effects. *Advances in Food and Nutrition Research*, *49*, 93–135. doi:10.1016/S1043-4526(05)49003-8
22. Younes, I., & Rinaudo, M. (2015). Chitin and chitosan preparation from marine sources. Structure, properties and applications. *Marine Drugs*, *13*(3), 1133–1174. doi:10.3390/md13031133
23. Di Martino, A., Sittinger, M., & Risbud, M. V. (2005). Chitosan: a versatile biopolymer for orthopaedic tissue-engineering. *Biomaterials*, *26*(30), 5983–5990. doi:10.1016/j.biomaterials.2005.03.016
24. Anitha, A., Sowmya, S., Kumar, P. T. S., Deepthi, S., Chennazhi, K. P., Ehrlich, H., … Jayakumar, R. (n.d.). Chitin and chitosan in selected biomedical applications. *Progress in Polymer Science*, *39*(9), 1644–1667. doi:10.1016/j.progpolymsci.2014.02.008
25. VandeVord, P. J., Matthew, H. W. T., DeSilva, S. P., Mayton, L., Wu, B., & Wooley, P. H. (2002). Evaluation of the biocompatibility of a chitosan scaffold in mice. *Journal of Biomedical Materials Research*, *59*(3), 585–590.
26. Francis Suh, J.-K., & Matthew, H. W. T. (2000). Application of chitosan-based polysaccharide biomaterials in cartilage tissue engineering: a review. *Biomaterials*, *21*(24), 2589–2598. doi:10.1016/S0142-9612(00)00126-5
27. Dutta, P. K. (Ed.). (2016). *Chitin and Chitosan for Regenerative Medicine*. New Delhi: Springer India. doi:10.1007/978-81-322-2511-9
28. Chedly, J., Soares, S., Montembault, A., von Boxberg, Y., Veron-Ravaille, M., Mouffle, C., Nothias, F. (2017). Physical chitosan microhydrogels as scaffolds for spinal cord injury restoration and axon regeneration. *Biomaterials*, *138*, 91–107. doi:10.1016/j.biomaterials.2017.05.024
29. Ladet, S. G., Tahiri, K., Montembault, A. S., Domard, A. J., & Corvol, M.-T. M. (2011). Multi-membrane chitosan hydrogels as chondrocytic cell bioreactors. *Biomaterials*, *32*(23), 5354–5364. doi:10.1016/j.biomaterials.2011.04.012
30. Shi, C., Zhu, Y., Ran, X., Wang, M., Su, Y., & Cheng, T. (2006). Therapeutic potential of chitosan and its derivatives in regenerative medicine. *The Journal of Surgical Research*, *133*(2), 185–192. doi:10.1016/j.jss.2005.12.013
31. Madihally, S. V., & Matthew, H. W. (1999). Porous chitosan scaffolds for tissue engineering. *Biomaterials*, *20*(12), 1133–1142.
32. Montembault, A., Viton, C., & Domard, A. (2005). Rheometric study of the gelation of chitosan in aqueous solution without cross-linking agent. *Biomacromolecules*, *6*(2), 653–662. doi:10.1021/bm049593m

33. Malaise, S., Rami, L., Montembault, A., Alcouffe, P., Burdin, B., Bordenave, L., David, L. (2014). Bioresorption mechanisms of chitosan physical hydrogels: a scanning electron microscopy study. *Materials Science & Engineering. C, Materials for Biological Applications*, *42*, 374–384. doi:10.1016/j.msec.2014.04.060
34. Yang, G., Yang, X., Zhang, L., Lin, M., Sun, X., Chen, X., & Gou, Z. (2012). Counterionic biopolymers-reinforced bioactive glass scaffolds with improved mechanical properties in wet state. *Materials Letters*, *75*(Supplement C), 80–83. doi:10.1016/j.matlet.2012.01.122
35. Yao, Q., Nooeaid, P., Roether, J. A., Dong, Y., Zhang, Q., & Boccaccini, A. R. (2013). Bioglass®-based scaffolds incorporating polycaprolactone and chitosan coatings for controlled vancomycin delivery. *Ceramics International*, *39*(7), 7517–7522. doi:10.1016/j.ceramint.2013.03.002
36. Liverani, L., Roether, J. A., Nooeaid, P., Trombetta, M., Schubert, D. W., & Boccaccini, A. R. (2012). Simple fabrication technique for multilayered stratified composite scaffolds suitable for interface tissue engineering. *Materials Science and Engineering: A*, *557*(Supplement C), 54–58. doi:10.1016/j.msea.2012.05.104
37. Mano, J. F., Hungerford, G., & Gómez Ribelles, J. L. (2008). Bioactive poly(L-lactic acid)-chitosan hybrid scaffolds. *Materials Science and Engineering: C*, *28*(8), 1356–1365. doi:10.1016/j.msec.2008.03.005
38. Zocca, A., Franchin, G., Elsayed, H., Gioffredi, E., Bernardo, E., & Colombo, P. (2016). Direct Ink Writing of a Preceramic Polymer and Fillers to Produce Hardystonite ($Ca_2ZnSi_2O_7$) Bioceramic Scaffolds. *Journal of the American Ceramic Society*, *99*(6), 1960–1967. doi:10.1111/jace.14213
39. Buffiere, J.-Y., Maire, E., Adrien, J., Masse, J.-P., & Boller, E. (2010). In Situ Experiments with X ray Tomography: an Attractive Tool for Experimental Mechanics. *Experimental Mechanics*, *50*(3), 289–305. doi:10.1007/s11340-010-9333-7
40. Ramirez Caballero, S.S. , Saiz, E., Montembault, A., Tadier, S., Maire, E., David, L., Delair, T., & Grémillard, L. (2019). 3-D printing of chitosan-calcium phosphate inks: rheology, interactions and characterization. *Journal of materials science: Materials in medicine 30:6*. doi: 10.1007/s10856-018-6201-y
41. Bakhsheshi-Rad, H. R., Hamzah, E., Kasiri-Asgarani, M., Jabbarzare, S., Daroonparvar, M., & Najafinezhad, A. (2016). Fabrication, degradation behavior and cytotoxicity of nanostructured hardystonite and titania/hardystonite coatings on Mg alloys. *Vacuum*, *129*(Supplement C), 9–12. doi:10.1016/j.vacuum.2016.03.021